

Symmetry-protected hierarchy of anomalous topological multipoles in wallpaper metacrystals

Xiujuan Zhang^{1*}, Zhi-Kang Lin^{2*}, Hai-Xiao Wang^{2,3*}, Zhan Xiong², Yuan Tian¹, Ming-Hui Lu^{1,4†}, Yan-Feng Chen^{1,4†} & Jian-Hua Jiang^{2†}

¹*National Laboratory of Solid State Microstructures, & Department of Materials Science and Engineering, Nanjing University, Nanjing 210093, China*

²*School of Physical Science and Technology, & Collaborative Innovation Center of Suzhou Nano Science and Technology, Soochow University, 1 Shizi Street, Suzhou 215006, China*

³*Department of Physics, Guangxi Normal University, Guilin 541004, China*

⁴*Jiangsu Key Laboratory of Artificial Functional Materials, & Collaborative Innovation Center of Advanced Microstructures, Nanjing University, Nanjing 210093, China.*

*These authors contributed equally to this work.

†Corresponding authors: jianhuajiang@suda.edu.cn, luminghui@nju.edu.cn and yfchen@nju.edu.cn

Symmetry and topology are two fundamental aspects of quantum states of matter such as the quantum Hall effects. Band topology is often characterized by symmetry-protected quantization of Berry's phases in wavevector space and is related to the quantum theory of polarization in crystals through the Bloch-Wannier representation. Recently, a new class of topological materials, higher-order topological insulators, were proposed and discovered, featuring bulk-edge-corner or bulk-surface-hinge correspondence that goes beyond the conventional topological paradigm. A prototype is an insulator with a topological quadrupole moment quantized by mirror symmetries, which leads to gapped edge states and in-gap corner states. However, the existing quadrupole topological insulators are based on a fine-tuned π -flux lattice model which does not directly illustrate the interplay between symmetry and topology. Here, using tunable acoustic metacrystals, we discover experimentally that the “wallpaper” $p4g$ crystalline group leads to a symmetry-protected hierarchy of topological Wannier multipoles: the lowest band gap has a quantized Wannier dipole and can mimic the quantum spin Hall effect, while the second band gap gives an anomalous topological quadrupole and the bulk-edge-corner correspondence. Such a topological hierarchy can be annihilated by tuning the metacrystal through a geometry transition from the $p4g$ wallpaper group to the C_{4v} point group, hence demonstrating elegantly the fundamental relation between symmetry and topology. The anomalous quadrupole moment originates from the intriguing topological structure in the Wannier representation as enriched by the nonsymmorphic wallpaper $p4g$ group. Through the symmetry-protected topological hierarchy, we observe experimentally multiplexing topological phenomena of distinct nature by changing the acoustic frequency,

since there is no band-filling issue in acoustics. Our study demonstrates an instance that classical systems with controllable geometry can serve as powerful simulators for the discovery of novel topological states of matter and their phase transitions.

Symmetry and topology are two fundamental paradigms in the classification of matters. The fundamental interplay and relation between symmetry and topology have been intriguing for physicists for decades, since the discovery of the quantum Hall effects. Historically, the first model demonstrating the beautiful relation between symmetry and topology is the Su-Schrieffer-Heeger model ¹ which shows that quantized dipole polarization of an insulator due to inversion symmetry has nontrivial consequences on the edges ² and serves as a fundamental example of charge fractionalization due to symmetry and topological principles ³.

In quantum mechanics, the bulk dipole polarization of a crystalline insulator is quantified through the Berry phase of the filled Bloch bands ^{4,5}. In the Bloch-Wannier representation, such a dipole polarization is calibrated by the displacement of the Wannier center with respect to the center of the unit-cell. When generalized to two-dimensional (2D) and three-dimensional (3D) insulators, such quantum description of the dipole polarization can be connected, respectively, to the Hall conductance and magneto-electric polarizability which characterize the topological responses of the 2D quantum Hall insulators and the 3D time-reversal invariant topological insulators, respectively ⁶⁻⁸. Recently, quadrupole and octupole topological insulators were proposed ^{8,9}, which extend band topology from dipole polarization to quadrupole and octupole polarizations in the Bloch-Wannier representation. For instance, a 2D quadrupole topological insulator (QTI) ⁸⁻¹² sup-

ports gapped edge states with quantized edge polarizations and in-gap, degenerate corner states at the edge-terminating corners, demonstrating the higher-order band topology ⁸⁻²³. A hallmark of the quadrupole topology is that, counter-intuitively, the corner charge is not an additive function of the edge polarizations but determined solely by the bulk quadrupole moment. As a consequence, each corner hosts only one localized mode with a fractional charge of $\frac{1}{2}$, despite that the polarizations of the edges terminated at the corner add up to a trivial corner charge of 0 ^{8,9}.

The emergence of a topological quadrupole moment in a crystalline insulator requires a few fundamental conditions. In the literature ^{8-12,23}, these conditions are: (i) a pair of mirror symmetries that quantize the dipole and quadrupole moments and make the former vanishing, and (ii) at least two occupied bands for the realization of cancelling dipole moments. The existing formulation of QTIs is based on a square-lattice tight-binding model with π -flux per plaquette, which needs both positive and negative couplings. Although the quadrupole moment is quantized by the mirror symmetries, without the π -flux per plaquette, the quadrupole moment always vanishes ^{8,9}. Therefore, this fine-tuned model is not an excellent manifestation of the fundamental interplay between symmetry and topology, although it is a seminal model that realizes the QTI. Because of its fine-tuned nature, the model is difficult to be realized in solid-state materials and classical waves (except for a few well-engineered systems ¹⁰⁻¹²). The 3D octupole topological insulator is even more challenging to be realized due to its complicated tight-binding configurations.

In this article, using 3D-printed acoustic metamaterials with controllable geometry, we demonstrate a new pathway toward topological multipoles. We use a symmetry-based approach to achieve

such a goal, where the wallpaper $p4g$ crystalline symmetry plays an essential role. We find that 2D sonic crystals (SCs) with wallpaper $p4g$ symmetry can realize a symmetry-protected hierarchy of topological Wannier multipoles without fine-tuning (in fact, even without the guidance from any tight-binding model). In our wallpaper SCs, the lowest acoustic band gap has a quantized Wannier dipole, while the second acoustic band gap has an anomalous Wannier quadrupole which cannot be described by any existing theoretical model (but can be verified using Wannier bands and various other characteristics, see Supplementary Information and Ref. ⁴⁰). In the literature, topological dipole and quadrupole moments are quantized by mirror symmetries. Counterintuitively, here, these topological multipoles are quantized without mirror symmetry but by nonsymmorphic glide symmetries (combinations of mirror reflections and half-lattice translations). Moreover, the anomalous topological quadrupole moment can be annihilated when the symmetry of the SC is tuned from the nonsymmorphic $p4g$ wallpaper group (consisting of glide symmetries) to the C_{4v} point group (consisting of mirror symmetries) by controlling the geometry of the acoustic metacrystal. The topological quadrupole moment vanishes exactly at the symmetry transition point, which thus illustrates explicitly the fundamental interplay between the symmetry and topology. We observe for the first time the symmetry-protected hierarchy of topological multipoles in acoustic metacrystals by changing the acoustic frequency, which allows multiplexing topological phenomena as benefited by the fact that there is no fermionic band-filling in acoustic systems.

The square-lattice SC (with a lattice constant $a = 2$ cm) has four arch-shaped scatterers in each unit-cell which are made of photosensitive resin (bulk modulus 2765 MPa, mass density 1.3 g/cm³, serving as “hard walls” for acoustic waves). The SC is fabricated using the commercial

3D-printing technology (see Materials and Methods). The geometries of the four scatterers are identical and are characterized by the arch height h , the arm length l and the arm width w , which can be tuned to tailor the acoustic bands and their topology (Fig. 1a). Those scatterers are arranged in such a way that the SC has two orthogonal glide symmetries, $G_x = \{m_x|\tau_y\}$ and $G_y = \{m_y|\tau_x\}$ where $m_x := x \rightarrow \frac{a}{2} - x$, $m_y := y \rightarrow \frac{a}{2} - y$, $\tau_y := y \rightarrow y + \frac{a}{2}$ and $\tau_x := x \rightarrow x + \frac{a}{2}$ with a being the lattice constant. With the inversion \mathcal{I} (i.e., parity) and the C_4 rotation symmetries, the system has a nonsymmorphic wallpaper space group of $p4g$. Plastic cladding boards above and below the SC structure lead to a quasi-2D acoustic system, with acoustic dispersions very close to the 2D limit for the low-lying bands (see Supplementary Information for supporting data). The acoustic bands (Fig. 1b) are obtained by solving the acoustic wave equation, $\nabla^2 P = \frac{\rho}{\kappa} \frac{\partial^2}{\partial t^2} P$ (ρ and κ are the mass density and bulk modulus, respectively) for the acoustic pressure P , using a commercial finite-element software (see Materials and Methods). With excellent controllability and versatile measurement methods, macroscopic SCs have manifested themselves as an appealing platform for the study of topological phenomena in classical waves^{25–36}. Here, we exploit such advantages for the discovery of the symmetry-protected hierarchy of topological multipoles.

At this point, it is important to point out a number of nontrivial consequences of the $p4g$ wallpaper group symmetry. First, the glide symmetries result in band-sticking effects at Brillouin zone (BZ) boundaries^{37–40}, leading to double degeneracy for all Bloch bands on the MX and MY lines in the BZ (Fig. 1b). In this way, the glide symmetries “glue” the first and second (the third and fourth) bands together. Second, the parity operator \mathcal{I} is also connected to the glide operators, $\mathcal{I} = \tau_y^2 G_x G_y = \tau_x^2 G_y G_x$. With such a connection, the parity eigenvalues of the Bloch bands at the

high-symmetry points in the BZ are constrained by the glide symmetries. Such constraints have important consequences on the quantization of the dipole polarization which is determined by the parity eigenvalues at the high-symmetry points in the BZ. In a $p4g$ crystal, the dipole moment is quantized as $\mathbf{p} = (\frac{1}{2}, \frac{1}{2})$ if there are an odd number of bands with parity-inversion between the Γ and X points, whereas $\mathbf{p} = (0, 0)$ if there are an even number of such bands⁹. From Fig. 1b, we conclude that the first acoustic band gap has a quantized dipole moment of $\mathbf{p} = (\frac{1}{2}, \frac{1}{2})$, while the second acoustic band gap has a cancelled, vanishing dipole moment. The vanishing dipole moment provides a basis for the quadrupole moment. We prove in the Supplementary Information and Ref. ⁴⁰ that the quadrupole moment is also quantized by the glide symmetries. Essentially, the glide symmetries have the same effects as the mirror symmetries on the Wannier centers and polarizations, as they are mirror reflections followed by half-lattice translations. However, unlike the mirror symmetries which commute with each other (or anti-commute with each other, as in Ref. ⁹), the glide symmetries do not commute with each other, i.e., $G_x G_y \neq G_y G_x$. The non-commutativity enriches the structure of the Wannier representation and is crucial for the emergence of the quadrupole topology without fine-tuning (See Supplementary Information and Ref. ⁴⁰). As a consequence, the resultant anomalous QTI requires at least four bands below the topological band gap and thus a Wannier representation larger than that of the conventional QTIs which have only two bands below the topological band gap. These characteristics are distinctive for the anomalous QTI protected by the glide symmetries.

We use the Wannier bands^{8,9} to characterize the topological quadrupole moment. The Wannier bands are, e.g., the k_y dependence of the Wannier centers $\nu_x^{(n)}$ ($n = 1, 2, 3, 4$) which are ob-

tained through the Berry phases ϕ_n of the first four acoustic bands associated with the Wilson-loop in the BZ (k_x runs from 0 to $\frac{2\pi}{a}$, for each k_y), following the relation $\nu_x^{(n)} = \phi_n/2\pi$ (see Supplementary Information for calculation details). Therefore, the Wannier bands are modulo 1 quantities, since the Berry phases ϕ_n are modulo 2π quantities. In our wallpaper SCs, the Wannier bands are gapped and non-degenerate with two Wannier bands below (above) the polarization gap at $\nu_x = 0$, labeled as “1” and “2” (“3” and “4”) in Fig. 1c. The two Wannier bands below the polarization gap can form two different sectors: the “sum” sector which corresponds to the sum of the two Wannier bands (labeled as “1+2” in Figs. 1d and 1e), and the “difference” sector for the difference between them (labeled as “1-2” in Figs. 1d and 1e). Similarly, the sum and difference sectors can be defined for the two Wannier bands above the polarization gap (labeled as “4+3” and “4-3” in Figs. 1d and 1e). Interestingly, the difference sector has gapped Wannier bands (see “1-2” and “4-3” in Figs. 1d and 1e) and quantized nested Wannier bands, thus yielding a nontrivial quadrupole topological index $q_{xy} = \frac{1}{2}$ (see Supplementary Information for details and rigorous proof). In contrast, the sum sector has gapless Wannier bands and yields quantized, canceling dipole moments (note that the dipole moments in $1 + 2$ and $3 + 4$ sectors cancel with each other). These features signify a novel anomalous QTI protected by the $p4g$ wallpaper group, which has not yet been discovered. The intriguing nature of this anomalous QTI (Wannier bands and nested Wannier bands as well as their evolution and transitions, bulk-edge-corner correspondence, many-body quantum quadrupole operator and other properties) is elaborated detailedly in Supplementary Information and in Ref. ⁴⁰ using theoretical and numerical analyses.

To illustrate the relation between symmetry and topology in our acoustic metacrystals, we

study the topological phase transition for the second acoustic gap which is solely triggered by tuning the geometry of the metacrystal. As shown in Fig. 2a, the continuous geometry transition is as follows: first decrease the arch height h of the arch-shaped scatterers, then reduce the arm-length l of the scatterers, and finally increase the arm-width w of the scatterers. Along this transformation, at $h = 0$, the symmetry of the SC undergoes a transition from the nonsymmorphic $p4g$ wallpaper symmetry to symmorphic C_{4v} point group symmetry. Figure 2b gives the topological phase diagram of the acoustic metacrystal. Through the geometry transition from the $p4g$ wallpaper group to the C_{4v} point group, the second band gap undergoes a transition from a quadrupole topological band gap to gap closing. Figure 2b shows that the topological phase transition takes place at exactly the geometry transition point. Therefore, the phase diagram demonstrates directly the fundamental interplay between symmetry and topology in our SCs. Accompanying the topological transition, the corner states merge into the bulk bands at the topological transition point and disappear in the gapless region and trivially gapped region with vanishing quadrupole moment $q_{xy} = 0$. As shown in the Supplementary Information and Ref. ⁴⁰ the topological transition is also characterized by the close of the polarization gap in the Wannier bands, which confirms the quadrupole topological transition in an alternative way.

Experimentally, we fabricate several SCs with different geometries and measure the bulk band gap as well as the frequency of the corner states (if they exist). The detailed experimental measurements are illustrated in the Method section, and also in the Supplementary Information where more supporting data on the transmission spectra are provided. The evolution of the geometry of the SCs is illustrated in Fig. 2a, with a transition from the wallpaper $p4g$ symmetry to

the C_{4v} point group symmetry. The measured bulk band gaps (blue and gray points in Fig. 2b for upper and lower band-edges, respectively) for those SCs agree fairly well with the calculation. Both experiments and calculation show that the corner states merge into the bulk bands at exactly the topological transition point where the symmetry transition from $p4g$ group to C_{4v} group takes place. We also confirm experimentally that after entering into the gapless regime and reopening of the bulk band gap with trivial topology, the corner states do not appear again. This phase diagram thus confirms the connection between the bulk quadrupole topology and the emergence of the corner states in the acoustic metamaterials from both experimental and theoretical aspects.

We further study the topological transition via the local density of states for the corner, edge and bulk regions (these regions are defined in the inset of Fig. 2d; calculation details are given in the Supplementary Information). Figures 2c-2f present the evolution of the bulk, edge and corner densities of states following the geometry evolution illustrated in Fig. 2a (specifically, the patterns labeled by the red asterisks in Fig. 2a are studied). For the wallpaper $p4g$ SCs (Figs. 2c and 2d), there are distinctive features of the quadrupole topological band gap: the emergence of gapped edge states in the bulk band gap and the sharp peak of corner states within the edge gap. At the transition from the $p4g$ wallpaper symmetry to the C_{4v} point group symmetry, the bulk band gap closes and the corner feature becomes weak and mingles with the edge and bulk states (Fig. 2e). For the trivial band gap case (Fig. 2f), the edge density of states does not exhibit a spectral gap. Moreover, the ratio between the corner, edge and bulk densities of states is close to the ratio between the areas of the corner, edge and bulk regions (approximately 0.1:0.6:1) outside the bulk band gap. Within the bulk band gap, the ratio between the corner and edge states is close to the the

ratio between the areas of the corner and edge regions. These properties indicate that the corner and edge densities of states outside the bulk band gap are due to the bulk, extended states, while the corner density of states within the bulk band gap is associated with edge states spreading into the corner regions. The above spectral features verify that the second acoustic band gap of the C_{4v} SCs does not exhibit the quadrupole topology, which is distinct from the quadrupole topological band gap of the $p4g$ SCs.

We now confirm the symmetry-protected hierarchy of topological multipoles by experimental measurements of the topological edge and corner states. We first measure the edge states in the second acoustic band gap, which are induced by the topological quadrupole moment. Unlike electronic states in tight-binding models, here the acoustic waves propagate in the air regions among the plastic scatterers in our SCs. To ensure a physical edge, we introduce an air channel of width $0.25a$ between the SC and the hard-wall boundary made of photosensitive resin. This method is commonly used in the study of topological edge states in sonic crystals^{24,32,33,36}. The width of such an air-channel is so narrow that the waveguide effect of the air channel (which can appear only for frequencies larger than 34 kHz) is excluded for the emergence of the edge states. In fact, the edge and corner states emerge for other widths of the air-channel as well. For instance, for the SC in Fig. 1a the edge and corner states emerge for the air-channel of width ranging from $0.2a$ to $0.5a$. This demonstrates that the emergence of the corner states is insensitive to the width of the air-channel. However, the width of the air-channel does affect the frequency of the corner states. We determine the width of the air-channel to ensure that the corner states merge into the bulk bands precisely at the topological transition point. In this way, the geometry effect of the air-channel on

the topological phenomena is minimized.

The experimental dispersions of the edge states are derived from the Fourier transformations of the measured frequency-dependent acoustic pressure profiles along the edge (see Materials and Methods). The obtained edge dispersions agree fairly well with the calculation, demonstrating the emergence of gapped edge states due to quadrupole topology (Fig. 3a). In these measurements, the acoustic pressure profiles for the edge states are detected under the acoustic excitation from a point-like source located at the middle of the edge (Fig. 3b). The simulated acoustic pressure profile with a point source excitation under the same conditions is presented in Fig. 3c for comparison. The simulation and experiment exhibit good agreement with each other. The robustness of the edge states against disorder is studied via numerical simulations in the Supplementary Information. Interestingly, we find that the edge states carry finite orbital angular momenta (OAM), which are manifested in two complementary ways: the phase and energy-flow distributions of the acoustic pressure fields. The phase distributions exhibit phase singularities and phase vortices, indicating finite OAM. The two edge states (labeled by the red and blue dots in Fig. 3a), which are time-reversal partners, have opposite phase winding properties, indicating opposite OAM. In addition, the distributions of the energy-flow of the acoustic pressure fields (see Materials and Methods) also indicate the finite, opposite OAM for those edge states. Figure 3a also shows that the quadrupole topological gap ranges from 10.9 kHz to 15.7 kHz, reaching a gap-to-mid-gap ratio of 37%. Besides, the edge band gap ranges from 12.5 kHz to 15.3 kHz, with a band gap ratio of 20%. These giant topological gaps lead to very strong wave confinement and enhanced wave intensity for the edge and corner states.

We then measure the corner states in a box-shaped, finite-sized structure where the SC is surrounded by hard-wall boundaries (see the inset of Fig. 4a). The calculated acoustic spectrum near the edge band gap is shown in Fig. 4a. Four degenerate acoustic modes, with each of them localized at one of the four corners, emerge in the edge band gap (Figs. 4b and 4c). This is an important feature of the quadrupole topology ^{8,9}. The robustness of the corner states against disorder is studied detailedly in the Supplementary Information.

To confirm the coexistence of the bulk, edge and corner states in our acoustic system, we measure the frequency-resolved acoustic responses of three different types of pump-probe configurations. We denote these pump-probe configurations as the bulk-probe, edge-probe and corner-probe, separately (see the inset of Fig. 4b). The measured transmission spectra for those pump-probe configurations are shown in Fig. 4b, where we normalize the data to set the peaks of the three curves to unity. The peak of the corner-probe lies in the spectral gap of the edge-probe, while the peaks of the edge-probe lie in the spectral gap of the bulk-probe. In addition, the peak responses of the edge- and corner-probes are much stronger than the peak bulk response, reflecting the enhancement of the acoustic field intensity at the edges and corners due to the emergence of the edge and corner states. Bearing in mind that the second band gap has vanishing dipole polarization, those experimental observations are regarded as the key features of the nontrivial quadrupole band topology ^{8,9} in our SC. Besides, we also measure the acoustic pressure profile for one of the corner states at the peak frequency of the corner-probe. The measured acoustic pressure profile (Fig. 4c) agrees well with the theoretical acoustic pressure profile obtained from the eigen-mode calculation (Fig. 4d). Together with the pump-probe spectra, these measurements indicate that there is

only one localized mode at each corner, which is another key feature of the quantized quadrupole moment^{8,9}. Note that the measured transmission spectra in Fig. 4b exhibit a small frequency blue-shift, compared with the calculated acoustic spectrum in the 2D limit in Fig. 4a, which can be associated with the small fabrication imprecision (about ± 0.1 mm) and the quasi-2D nature of the experimental system.

We now show that the lowest acoustic band gap (i.e., the dipole topological gap) can mimic the quantum spin Hall effect (QSHE) and realize acoustic helical edge states. The double degeneracy at the BZ boundary induced by the glide symmetries provides an instrumental for mimicking pseudo-spin degeneracy in acoustic systems which have no internal spin (polarization) degree of freedom. As shown later, the acoustic pseudospins are emulated by the OAM of acoustic waves. Following the band-inversion picture in the Bernevig-Hughes-Zhang model for QSHE⁴¹, the non-trivial topology of the quantum spin Hall insulator is characterized by the parity inversion at the high-symmetry points in the BZ. In our SCs, the band-inversion can be controlled by rotating the scatterers around the center of each quarter of the unit-cell (see the inset in Fig. 5a for the definition of the rotation angle θ). Differing from Fig. 2, here, the rotation of the scatterers leads to a symmetry transition from the $p4g$ group to the pgg group.

The parity eigenvalues of the lowest two acoustic bands at the Γ , X, Y and M points are shown in Figs. 5a and 5b. We notice that the parity eigenvalues at the Γ point do not change with the rotation angle. Besides, the X (Y) point always has double degeneracy between two bands with opposite parities. The band-inversion with parity switch can take place only at the M point,

as shown in Fig. 5a. Such band-inversion happens when the rotation angles is an integer of 90° , where the odd- and even-parity bands become degenerate (Figs. 5a and 5b). Note that the flat dispersion along the ΓX and MY directions at the rotation angle $\theta = 90^\circ$ are due to the fact that the scatterers overlap with each other and form connected “hard-walls” along the y direction and forbids wave propagation along the x direction, making the dispersion along k_x flat. This feature, which disappear for smaller scatterers, is not essential for the QSHE as shown in the Supplementary Information.

Fig. 5a gives the topological phase diagram for the first acoustic band gap: For the rotation angle between 90° and 180° , the band-inversion at the M point gives rise to nontrivial band topology (i.e., the acoustic QSHE); In contrast, for the rotation angles between 0° and 90° , the parities at the Γ and M points are the same, indicating trivial band topology. The former is regarded as the topological phase because the Γ and M points have opposite parities^{6,7} for $90^\circ < \theta < 180^\circ$. Since the system always has the C_2 symmetry, the topological phase diagram has a periodicity of 180° . We further employ a Hamiltonian analysis of the acoustic bands near the M point using the $\mathbf{k} \cdot \mathbf{p}$ method, which reveals that the above two phases are similar to the QSHE and trivial phases in the Bernevig-Hughes-Zhang model⁴², respectively (see Supplementary Information). An alternative topological classification based on the concept of topological crystalline insulators is presented in the Supplementary Information (for both the first and the second band gaps).

The helical edge states emerge in the lowest acoustic band gap at the boundary between the SCs with distinct topology (i.e., QSHE and normal band gap), as shown in Fig. 5c. The calculated

and measured (using the same method as in Fig. 3) dispersions of the acoustic edge states are consistent with each other. It is noticed that the dispersions of the edge states are not well-captured for the low-frequency part. The reason is that the decreased group velocity of the edge states in the low-frequency section leads to longer propagation time and stronger propagation loss and thus yields reduced fidelity of the recorded real-space acoustic pressure profiles and the dispersions obtained from the Fourier-transformation of these profiles. The gapless nature of the acoustic helical edge states is guaranteed by the glide symmetry on the edge which protects the double degeneracy at the $k_y = \frac{\pi}{a}$ point (see Supplementary Information for details)²¹. The robustness of the edge states is elaborated via numerical simulations in the Supplementary Information. The pseudospin-momentum-locking feature of the edge states is illustrated in Fig. 5d, where both the phase vortices and the rotating energy-flow in the acoustic pressure profiles indicate the finite OAM of the edge states. The acoustic OAM emulate the pseudospins in the acoustic helical edge states and time-reversed states have opposite pseudospins. Besides, simulation also confirms that the edge states support one-way transport when excited by acoustic sources with finite OAM (i.e., pseudospin-selective excitations, see Supplementary Information).

Beside its significance in fundamental science, the symmetry-protected hierarchy of topological multipoles in wallpaper metacrystals is also of central importance in material science. Since our symmetry-based approach can realize multipole topological band gaps without fine-tuning (in fact, even without relying on any tight-binding or lattice model), it greatly reduces the difficulties and opens more possibilities in realizing multipole topological phenomena and in exploiting such phenomena for the practical applications, such as integrated topological waveguides (edge states)

and cavities (corner states). Multiplexing topological phenomena in the two topological band gaps can considerably increase the capacity of topologically-protected information processing in a single chip. With the additional advantage that the topological band gaps can be very large, our symmetry-based approach provides an appealing pathway toward multipole topological insulators which can be generalized to other physical systems (e.g., photonic systems). In addition, our study establishes a bridge between subwavelength metamaterials (artificial functional materials that are useful for a broad range of applications) and topological multipole moments without relying on tight-binding pictures which are often absent in these metamaterials. When generalized to 3D systems, our symmetry-based approach may offer a possible route towards octupole topological insulators, a novel topological state of matter yet to be discovered.

Materials and Methods

Experiments

Our SCs consist of arch-shaped scatterers made of photosensitive resin (modulus 2765 MPa, density 1.3 g/cm³). A stereo lithography apparatus (with a fabrication tolerance of roughly 0.1 mm) is utilized to fabricate the samples. The vertical height of the sample is 1 cm. Two acoustic hard boards are used for cladding from the top and the bottom of the sample to form quasi-2D acoustic systems for the frequency range of interest (i.e., less than 20 kHz). The measured edge-state dispersions are obtained by the following procedure. We first scan the acoustic pressure field distribution along the edge for mono-frequency excitations. An acoustic transducer is placed under the sample to generate acoustic waves, which are further guided into the sample through an open

channel (with a diameter of 4 mm) at the bottom of the waveguide. The channel is located at the center of the edge (marked by the red star in Fig. 3B). An acoustic detector (B&K-4939 1/4-inch microphone), whose position can be controlled by an automatic stage, is used to probe the spatial dependence of the acoustic pressure from a circular open window (with a diameter slightly larger than the detector) on the top of the cladding layer. The data are collected and analyzed by a DAQ card (NI PCI-6251). The measured acoustic pressure profiles at different frequencies are then Fourier-transformed to obtain the edge-state dispersions. The Fourier transformation is implemented by using the Matlab built-in function *fft*. The transmission measurements are performed using a similar set-up, but with fixed positions of the source and the detector when the frequency is varied.

In the experimental measurements, the upper board of the waveguide (which is attached to an automatic stage) is required to be able to move freely, but without affecting the stabled samples, in order to record the acoustic pressure filed data. To accomplish this goal, we leave a tiny air gap (about 1 mm) between the upper board and the samples below it. This treatment might affect our measurements and could be another reason (additional to the fabrication imperfection) that the measurements are slightly deviated from the simulations on frequencies. Additionally, the condition for the environment atmosphere that varies upon weather change might also affect the sound speed and the air mass density and is the third reason to the frequency shift between the experiments and the simulations.

The transmission spectra presented in Fig. 4b are normalized by the maximum of each mea-

surement (i.e., the bulk-probe, edge-probe and corner-probe, respectively), so that they can be plotted at the same quantitative scale. The original, un-normalized transmission spectra are presented separately in the Supplementary Information. We find that the corner-probe yields a much stronger signal, more than 80 times stronger than the bulk-probe, indicating very strong enhancement of the acoustic wave intensity due to the strongly localized, subwavelength corner mode.

Simulation Numerical simulations are performed using a commercial finite-element simulation software (COMSOL MULTIPHYSICS) via the acoustic module. The resin objects are treated as hard boundaries. In the eigen-value calculations, the Floquet periodic boundaries are implemented. The projected band structures of the ribbon-like supercells and the band spectrum of the box-shaped supercell are calculated by setting the truncation boundaries as hard boundaries. For the simulated acoustic-pressure distributions of the edge and corner states, the frequency-domain study is performed. A point source, located at the center of the edge (near the corner), is utilized to excite the edge (corner) states. The energy flow is calculated through the time-averaged Poynting vector of the acoustic fields, following $\mathbf{S} = -(4\pi\rho f)^{-1}|P|^2\nabla\varphi$, where ρ is the density of air, f is the eigen-frequency, and $|P|$ and φ are the amplitude and the phase of the acoustic pressure profile, respectively.

References

1. Su, W. P., Schrieffer, J. R. & Heeger, A. J. Solitons in polyacetylene. *Phys. Rev. Lett.* **42**, 1698-1701 (1979).

2. Zak, J. Berry's phase for energy bands in solids. *Phys. Rev. Lett.* **62**, 2747-2750 (1989).
3. Jackiw, R. & Rebbi, C. Solitons with fermion number 1/2. *Phys. Rev. D* **13**, 3398-3409 (1976).
4. Resta, R. Macroscopic polarization in crystalline dielectrics: the geometric phase approach. *Rev. Mod. Phys.* **66**, 899-915 (1994).
5. Resta, R. Quantum-mechanical position operator in extended systems. *Phys. Rev. Lett.* **80**, 1800-1803 (1998).
6. Hasan, M. Z. & Kane, C. L. Colloquium: Topological insulators. *Rev. Mod. Phys.* **82**, 3045-3067 (2010).
7. Qi, X.-L. & Zhang, S.-C. Topological insulators and superconductors. *Rev. Mod. Phys.* **83**, 1057-1110 (2011).
8. Benalcazar, W. A., Bernevig, B. A. & Hughes, T. L. Quantized electric multipole insulators. *Science* **357**, 61-66 (2017).
9. Benalcazar, W. A., Bernevig, B. A. & Hughes, T. L. Electric multipole moments, topological multipole moment pumping, and chiral hinge states in crystalline insulators. *Phys. Rev. B* **96**, 245115 (2017).
10. Serra-Garcia, M. et al. Observation of a phononic quadrupole topological insulator. *Nature* **555**, 342-345 (2018).

11. Peterson, C. W., Benalcazar, W. A., Hughes, T. L. & Bahl, G. A quantized microwave quadrupole insulator with topological protected corner states. *Nature* **555**, 346-350 (2018).
12. Imhof, S. *et al.* Topoelectrical circuit realization of topological corner states. *Nat. Phys.* **14**, 925-929 (2018).
13. Noh, J. *et al.* Topological protection of photonic mid-gap defect modes. *Nat. Photon.* **12**, 408-415 (2018).
14. Schindler, F. *et al.* Higher-order topological insulators. *Sci. Adv.* **4**, eaat0346 (2018).
15. Langbehn, J., Peng, Y., Trifunovic, L., von Oppen, F. & Brouwer, P. W. Reflection-symmetric second-order topological insulators and superconductors. *Phys. Rev. Lett.* **119**, 246401 (2017).
16. Song, Z. D., Fang, Z. & Fang, C. (d-2)-dimensional edge states of rotation symmetry protected topological states. *Phys. Rev. Lett.* **119**, 246402 (2017).
17. Ezawa, M. Higher-order topological insulators and semimetals on the breathing Kagome and pyrochlore lattices. *Phys. Rev. Lett.* **120**, 026801 (2018).
18. Schindler, F. *et al.* Higher-order topology in bismuth. *Nat. Phys.* **14**, 918-924 (2018).
19. Xue, H., Yang, Y., Gao, F., Chong, Y. & Zhang, B. Acoustic higher-order topological insulator on a kagome lattice. *Nat. Mater.* **18**, 108-112 (2019).

20. Ni, X., Weiner, M., Alú, A. & Khanikaev, A. B. Observation of higher-order topological acoustic states protected by generalized chiral symmetry. *Nat. Mater.* **18**, 113-120 (2019).
21. Zhang, X. *et al.* Second-order topology and multidimensional topological transitions in sonic crystals. *Nat. Phys.* **15**, 582-588 (2019).
22. Khalaf, E. Higher-order topological insulators and superconductors protected by inversion symmetry. *Phys. Rev. B* **97**, 205136 (2018).
23. Franca, S., van den Brink, J. & Fulga, I. C. An anomalous higher-order topological insulator. *Phys. Rev. B* **98**, 201114 (2018).
24. Ma, G., Xiao, M. & Chan, C. T. Topological phases in acoustic and mechanical systems. *Nature Reviews Physics* **1**, 281-294 (2019).
25. Chen, Z. G. *et al.* Accidental degeneracy of double Dirac cones in a phononic crystal. *Sci. Rep.* **4**, 4613 (2014).
26. Yang, Z. J., Gao, F., Shi, X. H., Lin, X., Gao, Z., Chong, Y. D. & Zhang, B. L. Topological acoustics. *Phys. Rev. Lett.* **114**, 114301 (2015).
27. Xiao, M. *et al.* Geometric phase and band inversion in periodic acoustic systems. *Nat. Phys.* **11**, 240-244 (2015).

28. He, C., Ni, X. Ge, H., Sun, X. C., Chen, Y.-B., Lu, M.-H., Liu, X.-P. & Chen, Y.-F. Acoustic topological insulator and robust one-way sound transport. *Nat. Phys.* **12**, 1124-1129 (2016).

29. Lu, J., Qiu, C., Ye, L., Fan, X., Ke, M., Zhang, F., Liu, Z. Observation of topological valley transport of sound in sonic crystals. *Nat. Phys.* **13**, 369-374 (2017).

30. Xiao, M., Chen, W. J., He, W. Y. & Chan, C. T. Synthetic gauge flux and Weyl points in acoustic systems. *Nat. Phys.* **11**, 920-924 (2015).

31. Peng, Y. G., Qin, C. Z., Zhao, D. G., Shen, Y. X., Xu, X. Y., Bao, M., Jia, H. & Zhu, X. F. Experimental demonstration of anomalous Floquet topological insulator for sound. *Nat. Commun.* **7**, 13368 (2016).

32. Li, F. et al. Weyl points and Fermi arcs in a chiral phononic crystal. *Nat. Phys.* **14**, 30-34 (2017).

33. He, H. et al. Topological negative refraction of surface acoustic waves in a Weyl phononic crystal. *Nature* **560**, 61-64 (2018).

34. Wen, X., Qiu, C., Qi, Y., Ye, L., Ke, M., Zhang, F. & Liu, Z. Acoustic Landau quantization and quantum-Hall-like edge states. *Nat. Phys.* **15**, 352-356 (2019).

35. Peri, V., Serra-Garcia, M., Ilan, R. & Huber, S. D. Axial-field-induced chiral channels in an acoustic Weyl system. *Nat. Phys.* **15**, 357-361 (2019).

36. Yang, Y. *et al.* Topological triply degenerate point with double Fermi arcs. *Nat. Phys.* (2019).

37. Parameswaran, S. A., Turner, A. M., Arovas, D. P. & Vishwanath, A. Topological order and absence of band insulators at integer filling in non-symmorphic crystals. *Nat. Phys.* **9**, 299-303 (2013).

38. Wang, H.-X., Chen, Y., Hang, Z. H., Kee, H.-Y. & Jiang, J.-H. Type-II Dirac photons. *npj Quantum Mater.* **2**, 54 (2017).

39. Lin, J. Y., Hu, N. C., Chen, Y. J., Lee, C. H. & Zhang, X. Line nodes, Dirac points and Lifshitz transition in 2D nonsymmorphic photonic crystals. *Phys. Rev. B* **96**, 075438 (2017).

40. Lin, Z.-K., Wang, H.-X., Lu, M.-H. & Jiang, J.-H. Nonsymmorphic topological quadrupole insulator in sonic crystals. Preprint at <https://arxiv.org/abs/1903.05997> (2019).

41. Bernevig, B. A., Hughes, T. L., & Zhang, S.-C. Quantum spin Hall effect and topological phase transition in HgTe quantum wells. *Science* **314**, 1757-1761 (2006).

42. Fu, L. & Kane, C. L. Topological insulators with inversion symmetry. *Phys. Rev. B* **76**, 045302 (2007).

Acknowledgements X.J.Z, Y.T, M.H.L and Y.F.C are supported by the National Key R&D Program of China (2017YFA0303702, 2018YFA0306200, and the National Natural Science Foundation of China (Grant

No. 11625418 and No. 51732006). Z.K.L, H.X.W and J.H.J are supported by the Jiangsu Province Distinguished Professor Funding and the National Natural Science Foundation of China (Grant No. 11675116). J.H.J thanks Arun Paramekanti, Hae-Young Kee and Gil Young Cho for helpful discussions. He also thanks Sajeev John and the University of Toronto for hospitality where this work is finalized.

Author contributions J.H.J conceived the idea and initiated the project. J.H.J, Y.F.C and M.H.L guided the research. J.H.J, Z.K.L and H.X.W established the theory. Z.K.L, X.J.Z, X.Z and H.X.W performed the numerical calculations and simulations. X.J.Z and Y.T achieved the experimental set-up and measurements. X.J.Z, J.H.J and M.H.L performed data-analysis. All the authors contributed to the discussions of the results and the manuscript preparation. J.H.J, X.J.Z, Z.K.L and M.H.L wrote the manuscript.

Competing Interests The authors declare that they have no competing financial interests.

Data and materials availability All data are available in the manuscript and the Supplementary materials.

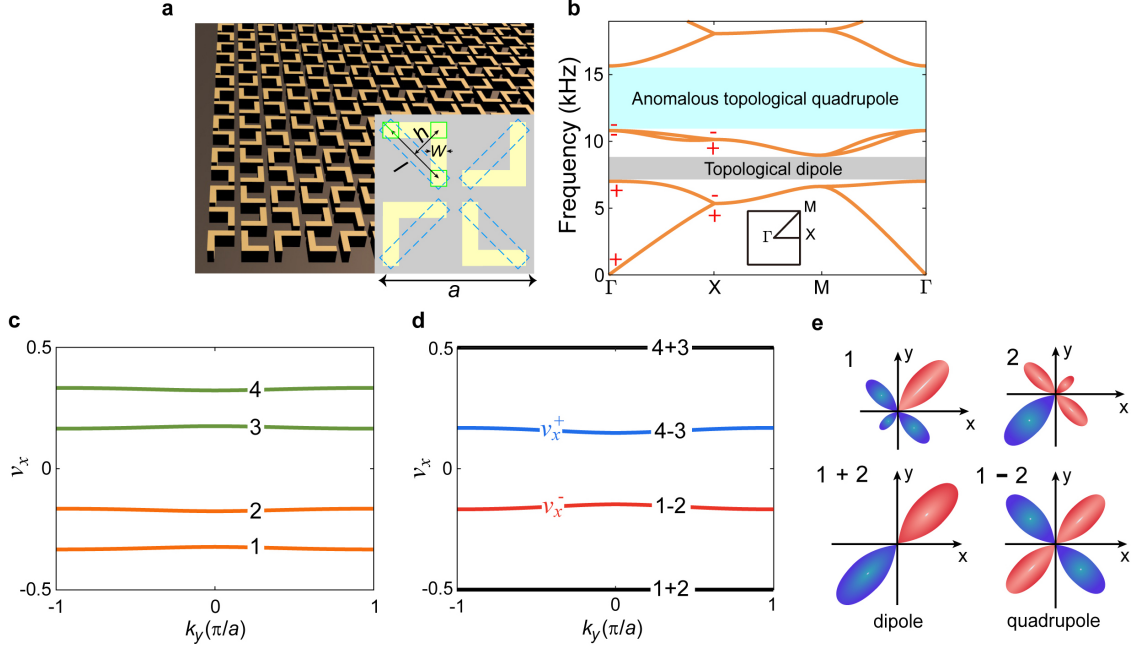


Figure 1 | Symmetry-protected hierarchy of anomalous topological multipoles in wallpaper

sonic crystals **a**, A bird's-eye view of the 2D wallpaper sonic crystal confined by plastic boards from below and above (not shown). Inset illustrates the unit-cell structure with four arch-shaped scatterers made of photosensitive resin using commercial 3D-printing technology. **b**, Acoustic bands and the hierarchy of multipole topological band gaps. The dipole and (anomalous) quadrupole are quantized and protected by the glide symmetries in the $p4g$ wallpaper group. Inset: Brillouin zone. Symbols +/- represent even/odd parity, respectively, at the Γ and X points in the Brillouin zone. **c**, Gapped and nondegenerate Wannier bands for the anomalous quadrupole topological gap. **d**, Wannier bands for the sum (“1+2” and “4+3”) and difference (“1-2” and “4-3”) sectors. **e**, Schematic illustration of a possible configuration of the Wannier orbits and their linear combinations in different sectors (“1+2” and “1-2”), which yields the anomalous quadrupole topology. Unit-cell geometry parameters are $h = 0.21a$, $l = 0.42a$, $w = 0.1a$ and $a = 2$ cm.

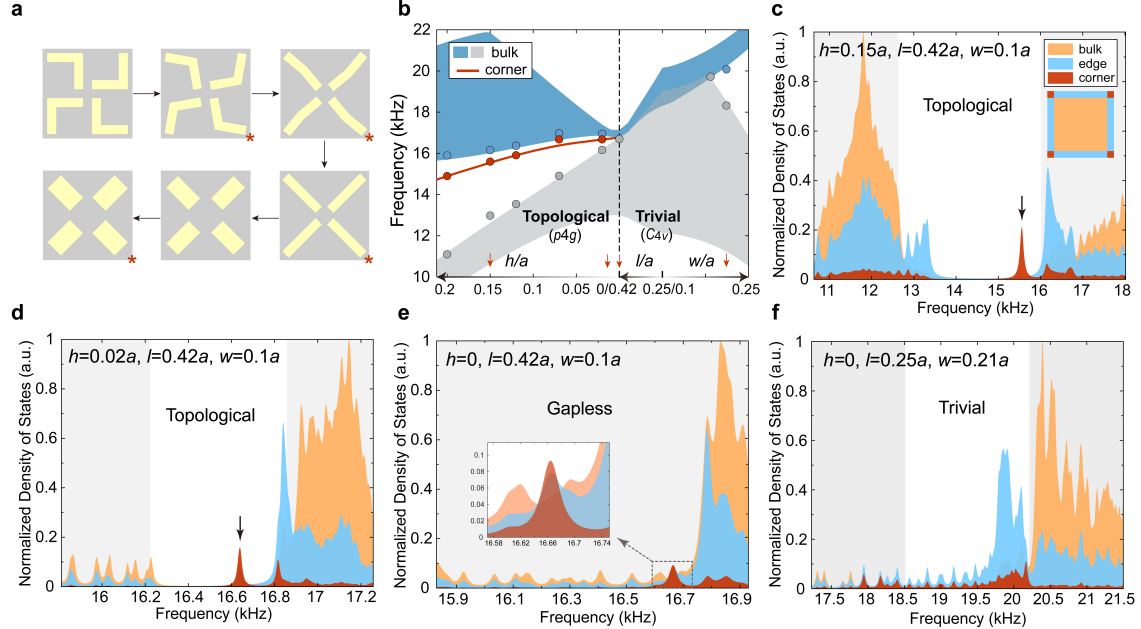


Figure 2 | Topological phase transitions in the second band gap. **a**, Topological phase transitions induced by continuously tuning the geometry: first decrease the arch height h , then reduce the length l , and finally increase the width w . Six geometries are used to illustrate the geometry transformation. **b**, Spectral signatures of topological phase transitions during the geometry transformation. Curves and areas are from simulations, while circles are from experiments. The bulk band gap closes at the geometry transition point from the $p4g$ wallpaper symmetry to the C_{4v} point group symmetry. The geometry transition point is exactly the topological phase transition point where the corner states merge into the bulk bands. After band gap closing and reopening, the corner states disappear in the trivial region. **c-f**, Calculated local density-of-states for the corner, edge and bulk regions are studied for our geometries labeled by the red asterisks in **a** and red arrows in **b**. The densities-of-states are normalized so that the peak values in the figures are 1. Here a.u. stands for arbitrary units. The corner, edge and bulk regions are sketched in the inset of **c**. The

experiments and calculations are performed on a box-shaped finite structure consisting of 10×10 sonic crystal unit-cells enclosed by hard-wall boundaries. An air channel of width $0.25a$ separates the sonic crystal and the hard-wall boundaries to ensure physical edges and corners for the acoustic waves (see details in Supplementary Information).

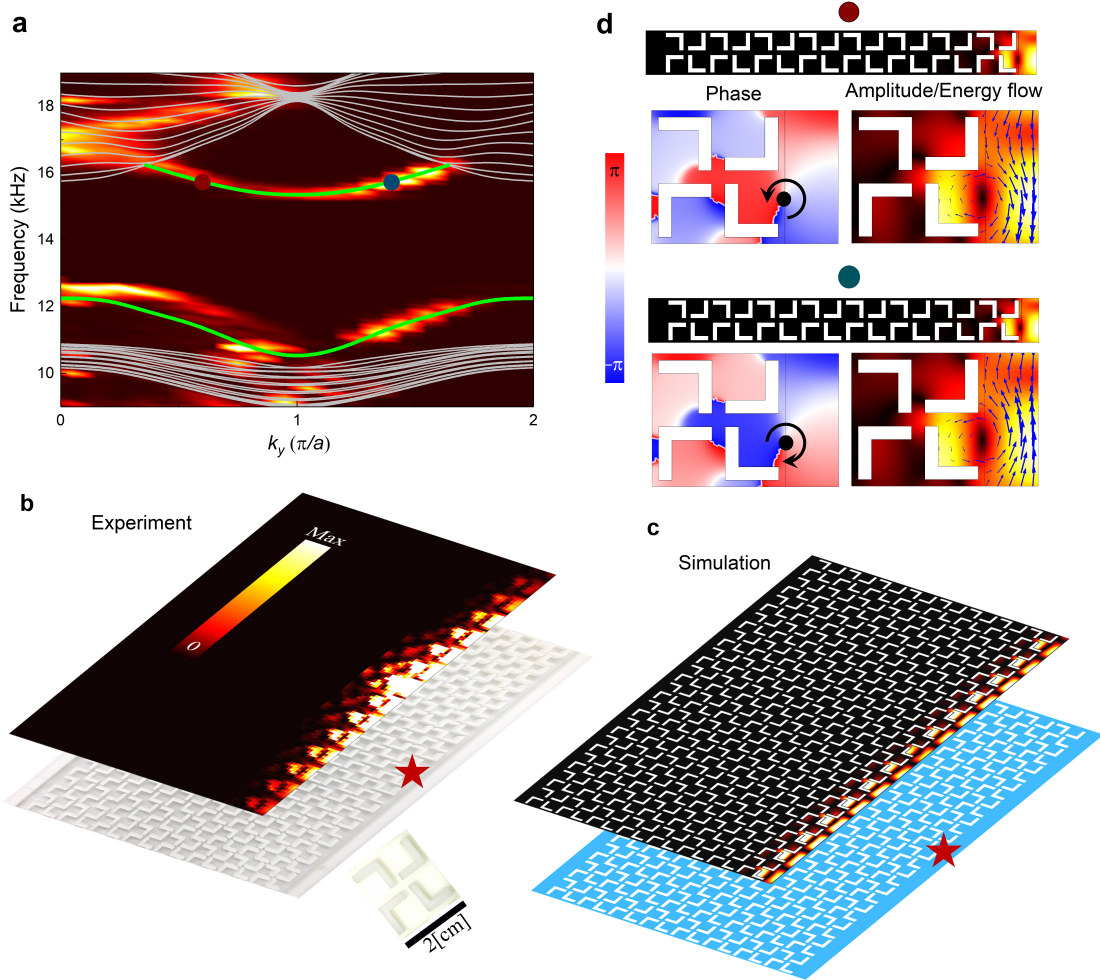


Figure 3 | Gapped topological edge states induced by anomalous quadrupole in the second band gap. **a**, Measured (hot color) and calculated (green) dispersions of the acoustic edge states. Gray curves represent calculated acoustic bulk bands. **b** and **c**, Top: measured and simulated acoustic pressure profiles of the edge states launched by a point-like source (indicated by the red stars), respectively; Below: photo of the fabricated sample and the illustration of the structure, respectively. Inset in **b**: photo of a unit-cell. **d**, Acoustic pressure profiles for the two edge states marked by the red and blue dots in **a**, with phase, amplitude and Poynting vectors (blue arrows)

shown near the edge. Phase vortex centers and phase winding directions are marked by the black dots and arrows, respectively. The edge is formed between the sonic crystal and the hard-wall boundary made of photosensitive resin. Unit-cell geometry parameters are the same as in Fig. 1.

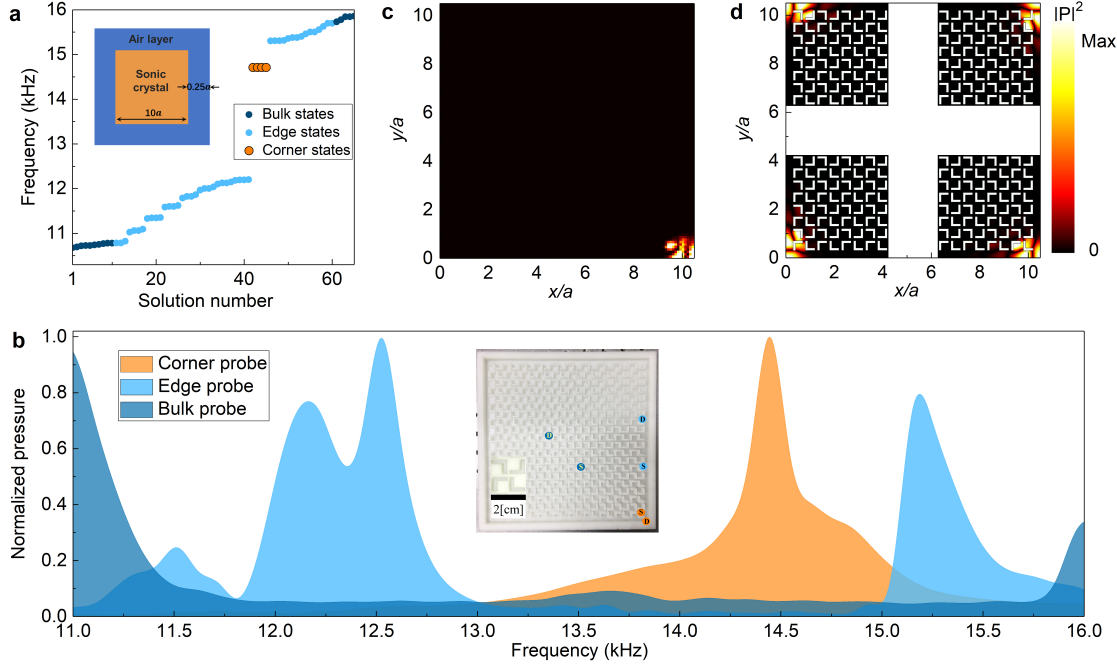


Figure 4 | Topological corner and edge states in the second band gap due to the anomalous quadrupole. **a**, Calculated acoustic spectrum for a box-shaped finite structure consisting of 10×10 sonic crystal unit-cells enclosed by hard-wall boundaries with an air channel of width $0.25a$ separating them. **b**, Frequency-resolved transmission spectra for three pump-probe configurations: bulk-probe, edge-probe and corner-probe. Inset: photo of the sample with a zoom-in photo of the unit-cell. Source “S” and detector “D” for each pump-probe configuration are marked in the inset using the same color as that of the corresponding transmission curve. **c** and **d**, Measured and simulated acoustic pressure profiles of the corner states, respectively. Four degenerate corner states (related by the C_4 rotation) are shown in **d**, while only one of them is measured in **c**. Unit-cell geometry parameters are the same as in Fig. 1.

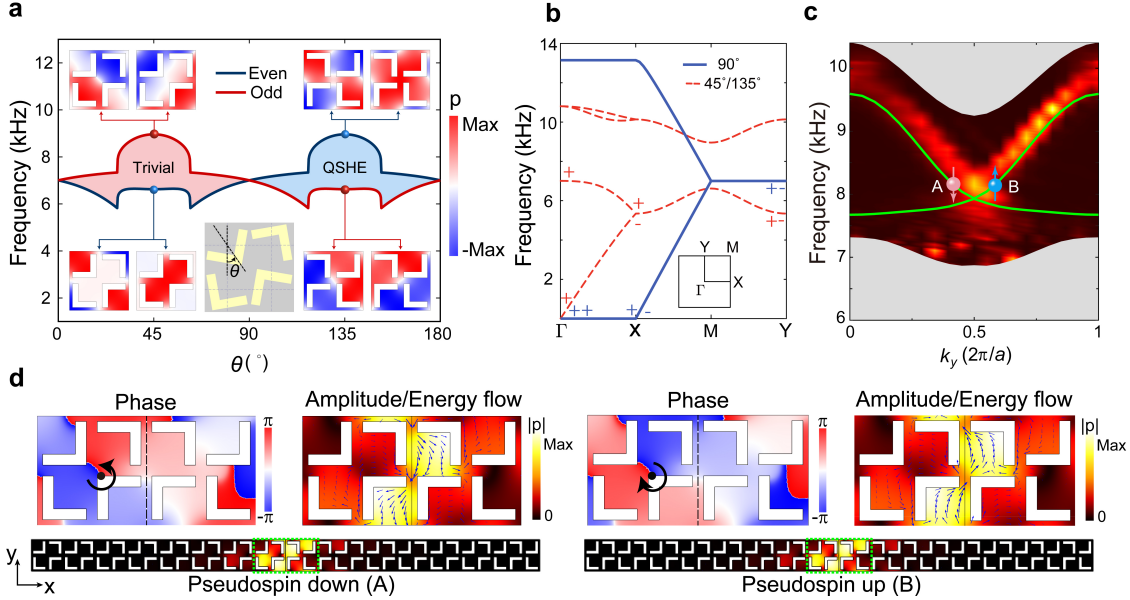


Figure 5 | Acoustic quantum spin Hall effect and helical edge states in the lowest band gap.

a, Evolution of the bulk bands and parities at the M point (including two doublets of even and odd parities) by tuning the rotation angle of the scatterers θ (defined in the inset). Acoustic pressure profiles of the doublets at the four marked points are shown as the insets. The parity-inversion indicates that the blue region mimics the quantum spin Hall insulator in acoustic systems, while the red region corresponds to trivial band gaps. **b**, Acoustic bands for $\theta = 90^\circ$, 45° and 135° . The symbols +/- represent, respectively, the even/odd parity for the Γ , X and Y points for the lowest two bands. The parities at the high-symmetry points in the Brillouin zone are used to determine the topological properties of the lowest band gap^{6,7}. **c**, Measured (hot color) and calculated (green) dispersions of helical edge states in the lowest band gap at the boundary between two sonic crystals with different θ 's, 45° and 135° . The gray regions denote the bulk bands. **d**, Acoustic pressure profiles for two edge states marked by the red and blue dots in **c**, with amplitude (hot color),

Poynting vectors (blue arrows) and phase profiles shown near the boundary (the green-box regions at the bottom pannel). Geometry parameters (except the rotation angle θ) are the same as in Fig. 1.